PHOTON OPTICS AT SCSS

M. Yabashi[1,2], T. Hirono[1,2], H. Kimura[1,2], H. Ohashi[1], S. Goto[1], S. Takahashi[1,2], K. Tamasaku[2], and T. Ishikawa[1,2]
[1] SPring-8/JASRI, Kouto 1-1-1, Sayo, Hyogo 671-5198, Japan
[2] SPring-8/RIKEN, Kouto 1-1-1, Sayo, Hyogo 671-5148, Japan.

Abstract

Vacuum ultraviolet (VUV) optics for the SCSS Prototype Accelerator (electron beam energy of $E_B = 250$ MeV) and X-ray optics for SCSS ($E_B = 8$ GeV) are summarized. The VUV optics have been designed for the diagnostics of the photon-beam properties in order to optimize the operation parameters of the accelerator. The system covers a radiation energy in the pulse from pJ to ≥ 10 μJ in the visible to VUV range. The first results were obtained during the commissioning period in the spring of 2006. In the latter part, R&D for x-ray free-electron laser (XFEL) optics at SPring-8 are introduced. Qualities of crystals, mirrors, and windows have been improved for coherent x-ray applications.

VUV OPTICS FOR SCSS PROTOTYPE ACCELERATOR

Introduction

The SCSS Prototype Accelerator [1] has been constructed for investigating fundamental performance of the accelerator system, which has been originally designed for the Japanese XFEL project, SCSS [2]. The Prototype machine is composed of a thermionic electron gun [3], an injector system, a main accelerator system with C-band linacs, and a couple of undulators. The undulators (with a period of 15 mm, a total period number of 600, and a minimum gap of 3 mm) produce VUV radiation with a wavelength range shorter than 60 nm at an electron beam energy of 250 MeV. Strong SASE radiation is emitted with the optimized operation conditions.

The photon diagnostics system has been constructed for the single-shot measurement of photon-beam properties such as spectrum, radiation energy, spatial profile. These parameters are crucial for studying accelerator conditions and for tuning SASE amplification. The system covers a wavelength range from visible (including a wavelength of 633 nm for the alignment with a He-Ne laser) to VUV light ($\geq$ 30 nm), and a radiation energy in the pulse from pJ (spontaneous radiation) to $\geq$10 μJ (SASE saturated radiation).

The system has been designed in the beginning of 2005, and installed during the summer construction period. The first beam of the visible light was observed in the end of November. After the replacement of some optical components, the system has been dedicated for the VUV diagnostics in the commissioning period from May to July of 2006. In particular, the first lasing was observed in June, 15th. After the first lasing, the beam tuning has been proceeded for optimizing SASE condition.

Design and Evaluation

General The schematic of the system is shown in Fig. 1. The components are placed on two granite tables, which are common designs to those used in the accelerator section. The beam pipes and components are evacuated with turbo-molecular pumps to a vacuum level of $\leq 10^{-6}$ Pa. Since the average power of the incident radiation is smaller than 1 mW at a maximum, cooling for optical components is unnecessary. A plane mirror (Au coating on a SiO_2 substrate for VUV; Al coating on a SiO_2 substrate for visible light) with a deflection angle of 170° is placed at the downstream of the first table for eliminating high-energy bremsstrahlung. A dispersive spectrometer, which is composed of an incident slit, a concave grating, and a charge-coupled device (CCD), is located in the second table. Several pneumatic actuators (indicated as monitors in Fig. 1) are prepared for inserting detectors, screens, and optical components in the beam path. At the upstream of the first table, a CCD camera and a movable plane mirror are installed for monitoring the He-Ne laser, which is used both for the alignment of the upstream components in the accelerator section and for this optical system.

Spectrometer The spectrometer is designed in a normal-incidence, constant-deviation geometry. The radius of the concave grating, the deflection angle, and the distance between the incident slit and the grating are $R = 922$ mm, $\gamma = 25°$, and $L_i = 1615$ mm, respectively. The wavelength λ focused in the center of the CCD is controlled by changing the incident angle of the grating, α, and the distance between the grating and the CCD, L_o, so as to satisfy the following equations simultaneously,

$$\frac{\cos^2\alpha}{L_i^2} + \frac{\cos^2(\alpha-\gamma)}{L_o^2} = \frac{\cos\alpha + \cos(\alpha-\gamma)}{R}, \quad (1)$$

and

$$\sin\alpha + \sin(\alpha-\gamma) = mN\lambda, \quad (2)$$

where m and N are the diffraction order and the line density of the grating, respectively. Two laminar gratings (Shimadzu Corp., Al coating with 600 lines/mm; Au coating with 2400 lines/mm) are prepared for covering longer ($\geq$ 100 nm) and shorter ($\leq$ 200 nm) wavelength region, respectively.

In the dispersed beam from the grating, different wavelengths are focused at different horizontal positions on the

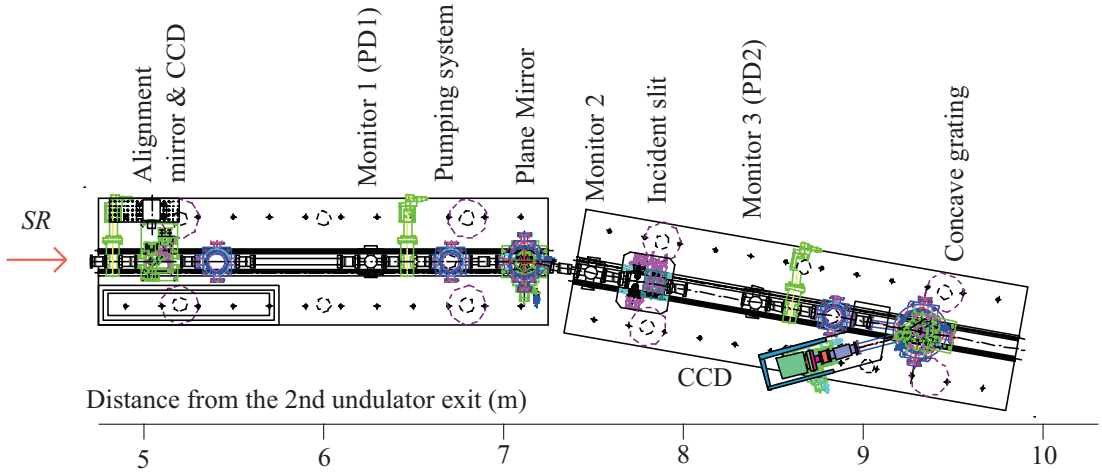

Figure 1: Layout of the optical system.

CCD. (Princeton Instruments Inc., PI-SX 400-1340B). The device, which has a back-illuminated sensor with electric cooling, covers from visible to the x-ray range. A pixel number and a pixel size are 1340 (h)×400 (v) and 20×20 μm^2, respectively. In the vertical direction, the concave grating simply works as a concave mirror. Thus, the vertical intensity distribution corresponds to a real image in the vicinity of the incident slit. An example of the spectrum image measured with the He lamp is shown in Fig. 2 (a).

The spectrum resolution is determined mainly from the following conditions: i) the line number in the illuminated area of the grating; ii) the spatial resolution of CCD; and iii) the aberration. Note that the incident beam to the slit is the quasi-plane wave, not focused as usual, because the plane mirror is used as a pre-optic. Thus the illuminated area on the grating is determined mainly by the beam divergence of the plane-wave diffraction at the slit.

Figure 3 shows calculated resolutions at a slit width of 100 μm and a detector resolution of 60 μm (3 pixels). The measured values using a helium lamp (He I, $\lambda = 58.43$ nm) and a mercury lamp (Hg I, $\lambda = 184.95$ and 253.65 nm) at the same slit width are also indicated in the figure. The measured results are mostly agreed with that calculated with the detector limitation. The resolution $\lambda/\Delta\lambda$ is grater than 1000 even at $\lambda = 58.4$ nm [see Fig. 2 (b)]. We note that a ray-trace calculation shows that the effect of the aberration is smaller than the other two factors. This result is supported by the experiment.

The spectrometer can be used for measuring a spatial profile at the slit position by switching the diffraction condition to the 0th order.

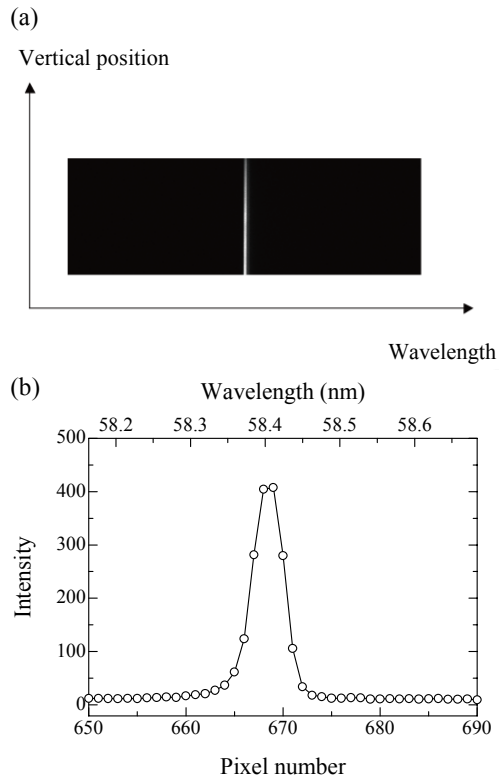

Figure 2: (a) Spectrum image measured with He lamp. The horizontal axis is the dispersive direction, where the right direction corresponds to longer wavelength. The vertical axis corresponds to the real image in the vicinity of the incident slit. (b) Intensity distribution along horizontal pixels, after the average over vertical pixels of (a). The upper axis shows the corresponding wavelength.

Intensity monitor Single-shot radiation intensities are measured with photodiodes, which are installed in the front of the mirror (PD1) and in the downstream of the slit (PD2). They are inserted to the beam axis by the remote control. The devices are designed for high-dose measurement (IRD Inc., SXUV100; SXUV100RPD [4]) with sensor sizes of 10x10 mm^2. The sensors are combined with a charge amplifier (PA-100) or with an oscilloscope. The gain of amplifier can be changed by a factor of 10^5. The signal is connected into the accelerator control system using an A/D

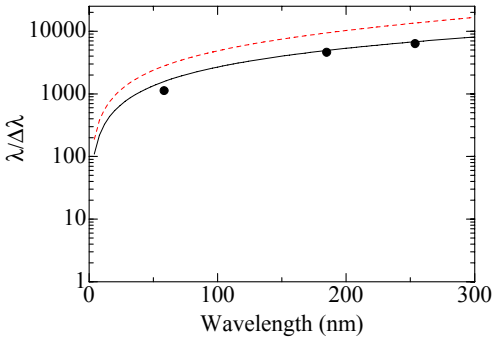

Figure 3: Resolution of spectrometer with a line density of grating of 2400 lines/mm. The dashed and solid lines are calculated results from the line number and the detector resolution, respectively. The solid circles are measured values.

converter.

Commissioning results

Spectrum Spectrum measurements for spontaneous and SASE radiations have been dedicated for tuning and evaluating the following conditions: i) optimization of electron-beam conditions including orbit, focusing, bunching condition, etc.; ii) tuning of undulators; iii) evaluation of the electron-beam density from SASE spectrum. In particular, the last [1].

The spectrum data are obtained typically with 100-shots accumulation for spontaneous light, and with single shot for SASE radiation. Figure 4 (a) shows a single-shot spectrum for SASE radiation at an electron charge of 0.24 nC, an undulator gap of 3 mm, and a slit width of 100 μm. The arc shape of the spectrum indicates that the wavelength tends to longer in the peripheral area, which is a similar phenomenon to the spontaneous radiation. The split into several lines are due to the fact that the beam is multimode. Figure 4 (b) shows a central, on-axis spectrum. The central wavelength is determined to be $\lambda = 59.0$ nm with a FWHM of $\Delta\lambda = 0.234$ nm.

The pulse length can be estimated from the spectrum. For example, if one assume that the pulse has a rectangular shape, the energy bandwidth ΔE and the pulse width Δt is represented as,

$$\Delta E \cdot \Delta t = 3.6\ (\mathrm{eV} \cdot \mathrm{fs}), \qquad (3)$$

in the Fourier-limited pulse. In our case, $\Delta E = 0.083$ eV is simply deduced from the relationship $\Delta E/E = \Delta\lambda/\lambda$. Then the pulse width is estimated to be $\Delta t = 43$ fs.

Radiation intensity The radiation intensities measured with photodiodes are particularly used for quick optimization of the operation parameters such as electron-beam orbit, bunching condition, timing, beam collimation, alignment of undulators, etc.

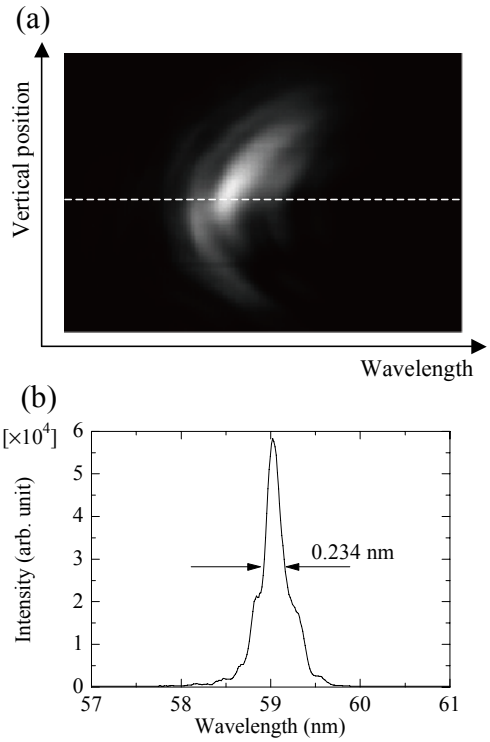

Figure 4: (a) Single-shot image of SASE radiation. (b) On-axis spectrum of (a) along the dased line.

The conversion from the output charge to the absolute intensity is necessary for evaluating SASE energy. At present, we use a catalog table [4] for refering the efficiency ($i.e.$, output charge of the detector per incident energy of the radiation pulse). However, it is desirable to determine the efficiency experimentally. For the purpose, we have tested a calibration method using the spontaneous radiation. First, the accelerator parameter is set to be debunching condition for producing only spontaneous radiation. Then the output charge per pulse is measured. The theoretical radiation energy to the detector is calculated using the sensor size and the distance to the detector. This partial energy has small dependences of machine parameters except the electron-beam energy and the charge. Thus the efficiency can be accurately obtained from the normalization of the measured charge by the calculated partial energy. The important point of the method is to choose moderate K parameter; the contamination of higher-order radiation is increased at a large K, while the dependence of the energy on K is too large at a small value. The optimized value is considered to be 0.2 to 0.7.

Figure 5 shows efficiencies of PD1 and PD2, measured with changing K parameter of the first undulator from 0.2 to 0.73. The catalog values are also indicated. The efficiency of PD1 is agreed with the catalog value within a 30 % deviation. Smaller values in PD2 are explained by the fact that PD2 is located in the downstream of the Au mirror, which has a reflectivity of ~ 80 %. Thus, it is plausible that the method can be applied to the quick check of

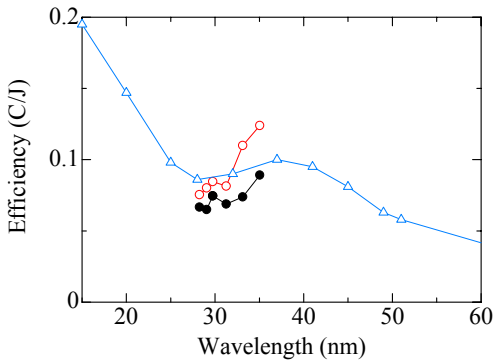

Figure 5: Detector efficiencies for PD1 (red open circles) and for PD2 (black closed circles). The blue open triangles show the catalog values.

the efficiency. We are planing to install thin-metal attenuators, because the present maximum energy, around 2 μJ, is nearly the saturation level of the detector. The above calibration method is effective even in this case. We note that the efficiencies in a wavelength range longer than 35 nm will be measured with low-energy operation of the accelerator.

Spatial profile and coherence The spatial profile at the slit position is measured using the 0th-order diffraction of the grating, where the grating simply works as a spherical mirror. Figure 6 (a) shows a single-shot image at a lasing condition only using the first undulator. The horizontal (vertical) width and divergence (in FWHMs) are determined to be 3.4 (3.9) mm and 240 (280) μrad, respectively, using a distance of 13.9 m from the undulator exit to the slit, as seen in Fig. 6 (b).

The spatial coherence is evaluated with a Young's double-slit experiment. The double slit with each width of 100 μm (height of 500 μm) and a central spacing of 400 μm were installed at the incident slit position. The grating was replaced with a plane mirror, and the diffraction image was recorded with the CCD, as shown in Fig. 7. The image with SASE radiation (single-shot detection) is compared to that at spontaneous radiation (100 shots). The former image has a higher visibility [Fig. 7 (c)], which indicate higher spatial coherence. We are planing to make more quantitative measurement using double slits with different spacings.

Extension for user experiment

In 2007, we are planning to start the operation dedicated for user experiments. A present plan for the extension is as follows: The experimental hall (about 12×8 m^2) is constructed at the outside of the accelerator tunnel. The beam transport channel is branched from the middle of the present diagnostic system. The beam is two-dimensionally collimated with double mirrors. A gas chamber with a differential pumping system is installed for a transparent, shot-by-shot monitor for the radiation intensity.

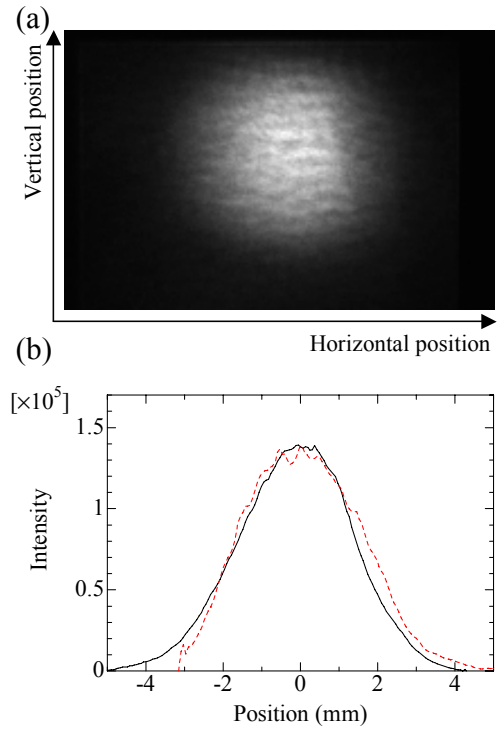

Figure 6: Spatial profile of SASE radiation (a), and its projections for horizontal (solid line) and the vertical (dashed line) axes (b).

X-RAY OPTICS FOR SCSS

Introduction

The principal missions of the optics in XFEL are i) to condition photon beam for user experiments, and ii) to diagnose radiation properties for the feedback to the accelerator. In this section, we will introduce R&D activities proceeded at SPring-8.

There are two technological challenges in XFEL optics. One is to suppress speckles possibly originating from imperfections of optical components under the coherent illumination. Both surface and bulk qualities should be strictly controlled.

The other is to keep the radiation dose below the melting limit [5, 6]. A simple solution is to extend the x-ray transport line for decreasing the energy density. However, in the SCSS case, the magnification of the beam area, when compared to that at the entrance of the beamline, is not larger than 10 because of small beam divergence (0.4 μrad at E=12.4 keV, for example) and the limited distance of $\sim$ 200 m. An alternative method is to use components made from light elements such as Be, B, C, etc. Figure 8 shows calculated doses for several materials that are placed normal to the incidence. The following beam parameters [2] are used for the calculation: the photon flux of 7.6×10^{11} photons/pls, the STD beam size at the source of 50 μmϕ, and the distance from the undulator exit of 100 m. The STD beam divergence is calculated from the diffrac-

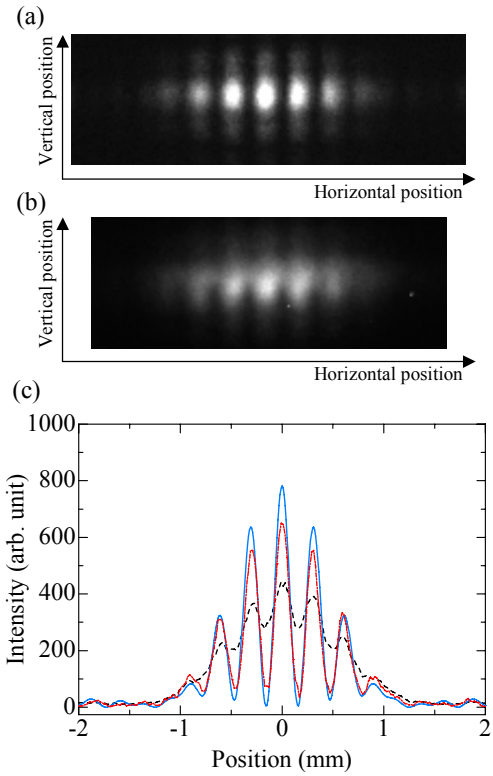

Figure 7: Young's double-slit experiment for SASE radiation with single shot (a), and for spontaneous radiation with 100 shots (b). The cross sections of the cental region at these conditions are shown in (c) as the red dot-dashed and black dashed line, respectively. A calculated result under the coherent illumination is also represented as a blue solid line.

tion limited condition for each photon energy. It is found that i) the doses of light materials (Be and C) have a margin to the threshold levels more than two-order of the magnitude, and ii) the dose of Si is still below the threshold, but iii) the dose of Cu is above threshold in the energy range higher than the K-absorption edge.

Crystals and windows

Crystal monochromator is used to set specific spectral window at SASE and spontaneous radiation. We have two candidates for crystal materials: Si and diamond. The energy resolutions ($\Delta E/E$) are 1×10^{-4} and 6×10^{-5} for Si (111) and Diamond (111) reflections, respectively.

Si is the most popular materials for monochromator crystal at the present synchrotron facilities, because of the availability of high-quality, large-volume ingots. Since the Bragg angle for (111) reflection at $E = 10$ keV is 11 degree, the dose per atom around this photon energy is decreased by a factor of 5, compared to the normal incidence case shown in Fig. 8. The ratio is further increased for higher photon energy (*i.e.*, lower Bragg angle). Thus, Si would be useful as XFEL monochromator above 10 keV. Crystal cooling is not a serious problem for SCSS. Because

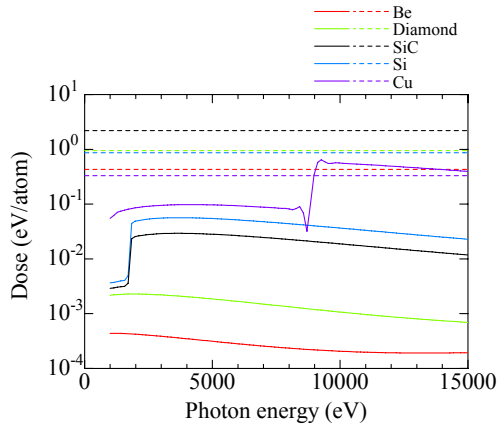

Figure 8: Energy dependence of dose for several materials. Solid lines are calculated values with SCSS beam parameters, while dashed lines are the threshold levels of melting limit.

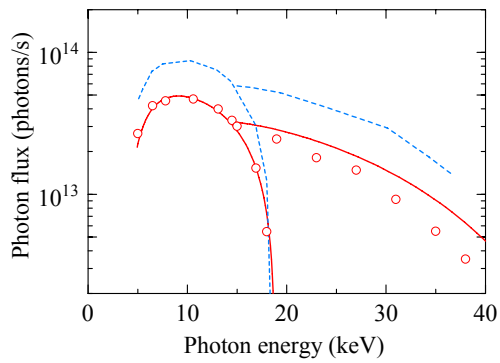

Figure 9: Photon flux of the monochromatic beam at SPring-8 undulator beamlines. The open circles and solid lines are measured and calculated values for diamond monochromator, respectively, and the dashed lines are measured values for cryogenically-cooled Si monochromator.

the average power is smaller than 100 mW, water cooling would be sufficient.

Diamond monochromator is the most promising when utilized under a higher dose. We have collaborated with Sumitomo Electric Industries Ltd. (SEI) to develop high-quality synthetic diamond in type IIa [7]. Recently, (111) crystal plates with relatively large sizes ($\sim 8 \times 4$ mm^2) are commercially available. We have tested performance of diamond double-crystal monochromator (DCM) at a SPring-8 undulator beamline. Two (111) diamonds crystals, which are attached to copper crystal holders using indium sheets, are cooled by water. Figure 9 shows the measured photon flux. Experimental results are well agreed with the theory in the energy range below 20 keV. Topographic studies showed a relationship between the surface condition and the image quality. It is necessary to develop surface polishing technique.

For windows, Be foils have been widely used at syn-

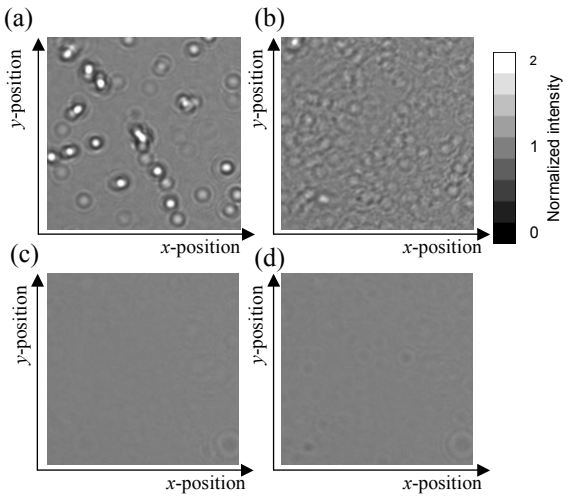

Figure 10: Transmission images of Be windows: Polished PF-60 (a), polished IF-1 (b), polished PVD (c), and Kapton foil (d). The photon energy is $E = 12.4$ keV. The beam areas are 300×300 μm^2. The distance between the sample to the camera is 1400 mm. The round spots commonly seen at the bottom-right corners of (c) and (d) are caused from a Kapton foil in the upstream of the system.

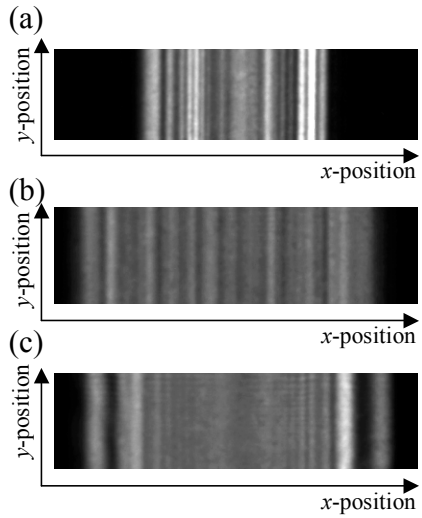

Figure 11: Reflection images of Si mirrors: Pre-machined surface (a), PCVM polished surface (b), and PCVM+EEM polished surface (c).

chrotron facilities owing to their low absorptions for x-rays. They are also promising candidates for XFEL windows from the viewpoint of the dose issue (see Fig. 8). However, it has been found that they produced speckles under coherent illumination. From the experiment at the 1 km beamline of SPring-8, it was found that the speckles in the conventional Be windows shown in Fig. 10 (a,b) are originated mainly from voids in the bulk [9]. To remove the voids, the physical vapor deposition (PVD) method has been tested. The surface of the PVD Be foil has been polished to decrease the surface roughness to be 0.05 μm. Finally, the image of a polished PVD Be shown in Fig. 10 (c) was found to be superior to that of a Kapton foil in (d) [10]. We note that Be will be useful for attenuators. Higher attenuation will be achieved using Si or SiC.

Mirror

Total-reflection mirrors are used for deflecting SASE radiation in order to eliminate high-energy bremsstrahlung. Focusing is another important function of the mirror. The surface quality is crucial for suppressing speckles under coherent illumination. From 2000, we have collaborated with Osaka University to realize high-quality mirrors. Special techniques of surface polishing have been developed: EEM (Elastic Emission Machining) and PCVM (Plasma Chemical Vaporization Machining) [11]. Figure 11 shows reflected images of Si mirrors measured at the 1 km beamline with a photon energy of $E = 20$ keV. The incident angles and the distance between the mirrors to the camera are set at 1.2 mrad and 966 mm, respectively. The intensity fluctuations observed with the pre-machined surface in Fig. 11 (a) are mostly suppressed with the PCVM+EEM polished mirror in (c). Thus, we can conclude that the mirror is available for conditioning coherent x-rays.

These machining techniques with combination of a new metrological method called the microstitching interferometry (MSI) [12] were applied to fabrication of aspherical mirrors for nano-focusing. A couple of Pt-coated mirrors are fabricated with figure accuracies of 2 nm (p-v). Two dimensional focusing down to 36×48 nm^2 has been achieved at $E = 15$ keV with the Kirkpatrick-Baez arrangement [13].

Another critical issue for the XFEL mirror is to choose appropriate surface material to suppress the dose under the melting limit [5]. Figure 12 shows the calculated doses and reflectivities for several materials. The beam parameters are as same as those used in Fig. 8 with a photon energy of $E = 12.4$ keV. It is found that C or SiC seems to be useful, while Si and Au are questionable. From the figure, the incident angles should be smaller than 2 mrad (0.14 degree). If we set an acceptance width to be 1 mm, the total length of the mirror should be larger than 500 mm. Thus, the next R&D issues for XFEL mirror fabrication are i) to study coating and polishing method for the light materials, and ii) to product large mirror with a sufficient figure accuracy. It is also important to establish technologies to protect the surface from contaminations or dusts, because small decrease of reflectivity can cause serious damage of the surface under the high-dose irradiation. Great care should be required in the design of the driving mechanism in order to keep an ultraclean environment.

Single-shot spectrometer

As shown in the previous section, the VUV single-shot spectrometer has played a central role for the radiation diagnostics. Development of similar instrument that works

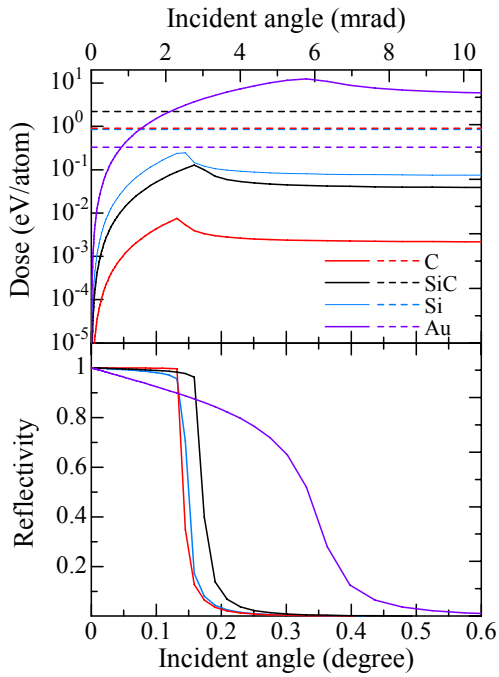

Figure 12: (above) Angular dependences of doses for the total reflection mirrors. Several materials are compared. Solid lines are calculated values with SCSS beam parameters, while dashed lines are the threshold levels of the melting limit. (below) Dependences of reflectivities.

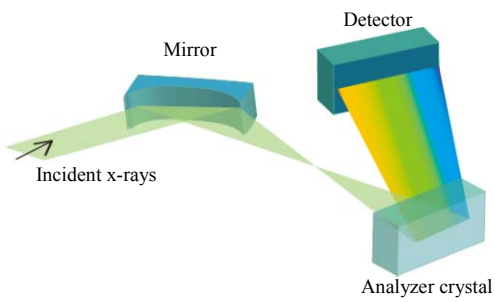

Figure 13: Setup for single-shot x-ray spectrometer.

in the x-ray region is crucial. Recently, we have developed such a spectrometer that combines a high-quality mirror and a Si flat crystal. The former is used to diverge the incident parallel beam, while the latter is to select specific energy according to the Bragg's law. As a result, the exit beam has an energy dispersion. The key point is again the figure accuracy of the mirror to suppress speckles. Using (555) reflection for the analyzer crystal, the energy resolution of the instrument has been measured to be 13.1 ± 1.9 meV at $E = 10$ keV with a full energy range of ~ 3 eV. Wider energy range can be easily obtained by changing diffraction plane to lower index [14].

SUMMARY

The VUV diagnostic system for the SCSS prototype accelerator has been constructed and successfully operated. At a lasing condition, a radiation energy in the pulse has been evaluated to be ~ 2 μJ. The pulse width is estimated to be shorter than 100 fs from the measurement of the energy spectrum. The double-slit experiment showed that higher spatial coherence is achieved at a lasing condition.

As XFEL optical components, we have developed high-quality diamonds, mirrors, and Be windows. A single-shot spectrometer for XFEL diagnostics has been tested and confirmed to have a high resolution of 1.3×10^{-6} at $E = 10$ keV.

ACKNOWLEDGEMENT

We thank all SCSS members for fruitful discussions and suggestions. We acknowledge Dr. Y. Takata (RIKEN), Dr. Y. Harada (RIKEN), and Dr. T. Tokushima (RIKEN) for their suggestions on designing the spectrometer, Dr. A. Higashiya (RIKEN), Dr. T. Matsushita (JASRI), Dr. Y. Tamenori (JASRI), and Dr. A. Sekiyama (Osaka Univ.) for their help in the calibration of the spectrometer, Mr. T. Kirimura (RIKEN) for the calibration of the photodiodes, Mr. M. Tanaka (JASRI), Mr. T. Irie (JASRI), and Mr. K. Onoe (ULVAC) for their activities in the installation of the VUV diagnostic system.

REFERENCES

[1] H. Tanaka et al., in these proceedings.

[2] "SCSS X-FEL Conceptual Design Report", RIKEN/SPring-8, May 2005, Mikazuki, Japan, http://www-xfel.spring8.or.jp/

[3] K. Togawa et al., "Emittance Measurement on the CeB_6 Electron Gun for the SPring-8 Compact SASE Source", FEL 2004 conf. proc. (2004) THBOC03.

[4] International Radiation Detector Inc., http://www.ird-inc.com/

[5] R. Tatchyn, "LCLS Optics: Technological Issues and Scientific Opportunities", SLAC-PUB-6064, SLAC, Stanford (1993).

[6] "Linac Coherent Light Source (LCLS) Conceptual Design Report", SLAC-R-593, SLAC, Stanford (2002).

[7] K. Tamasaku, T. Ueda, D. Miwa, and T. Ishikawa, "Goniometric and topographic characterization of synthetic IIa diamonds", J. Phys. D: Appl. Phys. **38** (2005) A61.

[8] M. Yabashi et al., "Diamond double-crystal monochromator for SPring-8 undulator beamlines", Proc. for SRI 2006 (in press).

[9] S. Goto, M. Yabashi, K. Tamasaku, S. Takahashi, and T. Ishikawa, "Characterization of Beryllium Windows using Coherent X-rays at 1-km Beamline", AIP conf. proc. **705** (2004) 405.

[10] S. Goto, M. Yabashi, K. Tamasaku, and T. Ishikawa, "Characterization of Beryllium Windows for Coherent X-ray Optics", Proc. for SRI 2006 (in press).

[11] Y. Mori et al., "Development of plasma chemical vaporization machining and elastic emission machining systems for coherent X-ray optics", Proc. SPIE, Vol. 4501 (2001) 30.

[12] K. Yamauchi et al., "Microstitching interferometry for x-ray reflective optics", Rev. Sci. Instrum. **74** (2003) 2894.

[13] H. Mimura et al., "Hard X-ray Diffraction-Limited Nanofocusing with Kirkpatrick-Baes Mirrors", Jpn. J. Appl. Phys., **44** (2005) L539.

[14] M. Yabashi et al., "Single-shot spectrometry for x-ray free-electron laser", Phys. Rev. Lett. **97** (2006) 084802.